Modeling and Measurements of Multiphase Flow and Bubble Entrapment in Steel Continuous Casting

KAI JIN, BRIAN G. THOMAS, and XIAOMING RUAN

In steel continuous casting, argon gas is usually injected to prevent clogging, but the bubbles also affect the flow pattern, and may become entrapped to form defects in the final product. To investigate this behavior, plant measurements were conducted, and a computational model was applied to simulate turbulent flow of the molten steel and the transport and capture of argon gas bubbles into the solidifying shell in a continuous slab caster. First, the flow field was solved with an Eulerian k–ε model of the steel, which was two-way coupled with a Lagrangian model of the large bubbles using a discrete random walk method to simulate their turbulent dispersion. The flow predicted on the top surface agreed well with nailboard measurements and indicated strong cross flow caused by biased flow of Ar gas due to the slide-gate orientation. Then, the trajectories and capture of over two million bubbles (25 μm to 5 mm diameter range) were simulated using two different capture criteria (simple and advanced). Results with the advanced capture criterion agreed well with measurements of the number, locations, and sizes of captured bubbles, especially for larger bubbles. The relative capture fraction of 0.3 pct was close to the measured 0.4 pct for 1 mm bubbles and occurred mainly near the top surface. About 85 pct of smaller bubbles were captured, mostly deeper down in the caster. Due to the biased flow, more bubbles were captured on the inner radius, especially near the nozzle. On the outer radius, more bubbles were captured near to narrow face. The model presented here is an efficient tool to study the capture of bubbles and inclusion particles in solidification processes.

DOI: 10.1007/s11663-015-0525-5

I. INTRODUCTION

ARGON bubbles captured during the continuous casting of steel are a major cause of defects, such as blisters and slivers, in rolled steel products.[1] Ar gas is usually injected at the slide gate or stopper rod to prevent nozzle clogging.[2–4] The jets of molten steel then carry those bubbles through the Submerged Entry Nozzle (SEN) and into the mold cavity region, where they greatly affect the flow pattern, surface level fluctuations, and slag entrainment. Large bubbles captured near the surface can lead to blister defects, such as pencil pipe, after rolling and annealing.[5,6] Furthermore, the moving Ar bubbles collect nonwetting inclusion particles, such as alumina. If such a bubble is captured by the solidifying steel shell, the layer of inclusions covering its surface will lead to large oxide clusters, which cause severe sliver defects in the final product.[7,8] Ar bubbles entering the mold region end up at three locations: (1) some reach the top surface, pass through the slag layer, and escape harmlessly to the atmosphere; (2) some are captured near the meniscus and lead to surface defects; (3) some are captured deep in the caster and cause internal defects.

Many previous works have studied two-phase flow of argon and molten steel in the SEN and mold region of the continuous caster using water models and computational models.[2,7–24] Increasing Ar gas causes increased upward flow near the SEN and tends to reverse the classic double-roll flow pattern to single roll with surface flows away from the SEN toward the narrow face.[10,19,20] Asymmetric, oscillating flow is observed if gas fractions are excessive.[2,25] Computational models of this multiphase flow should be three-dimensional and two-way coupled, as the Ar gas affects the steel flow and vice versa, especially with large gas fractions.[9–11,21]

Many researchers have used Eulerian–Eulerian flow models to investigate this two-phase flow problem.[10,18–20,26] Liu *et al.*[21] recently used inhomogeneous Multiple Size Group (MuSiG[27]) Eulerian models of the gas phase to describe the polydispersed bubbly flow in this process. Flow is affected by the input bubble size distribution. Liu *et al.* measured Sauter mean diameters (1 to 3 mm) in their physical water model, which are typical of previous measurements.[28] Increasing gas flow generates more and larger bubbles.[2,25,28] Argon bubbles in steel are reported to be larger than air bubbles in water.[21,28]

Other models have used Lagrangian descriptions for the argon gas bubbles[9–15,17,29] such as the Discrete

---

KAI JIN, Research Assistant, and BRIAN G. THOMAS, C.J. Gauthier Professor, are with the Department of Mechanical Science and Engineering, University of Illinois at Urbana-Champaign, 1206 West Green Street (MC-244), Urbana, IL, 61801. Contact e-mail: bgthomas@illinois.edu XIAOMING RUAN, Senior Researcher, is with the Steelmaking Research Department, Research Institute Baoshan Iron & Steel Co., Ltd., 889 Fujin Rd., Shanghai 201900, P.R. China.

Manuscript submitted September 28, 2015.

Particle Method (DPM) to study flow and bubble transport in the SEN and mold region.[11,13,16,17,29] Liu *et al.*[29] performed such Eulerian–Lagrangian two-way coupled k–ε simulations of Ar-steel flow with a coarse 0.15-million cell mesh. In the mold region, large bubbles (0.25 to 2.5 mm diameter) float directly upwards to the top surface upon exiting the SEN, while bubbles smaller than 0.25 mm travel with the jet across the mold cavity. A simple Eulerian–Eulerian model with a single equation set for the bubble phase misses this effect.

Relatively few previous flow studies have been extended to the important topic of motion and capture of particles, such as bubbles and inclusions.[11–17,21–24,29–31] The chaotic motion of individual particles in turbulent flow is automatically simulated by integrating the trajectories of large numbers of individual particles, as a post-processing step after large eddy simulations of the transient flow field on a refined mesh.[13,14,17] With steady Reynold-averaged Navier–Stokes (RANS) models, this particle dispersion behavior can be mimicked using the random walk method.[11,12,15–17,21–24,29–31]

To predict the capture of Ar bubble and/or inclusion particles, a suitable capture criterion is needed. Many previous works have investigated the behavior of a particle at a solidification front[32–39] including fundamental numerical studies with simplified conditions such as planar-front solidification[32–34,36–39] and initially stationary flow. Particles are pushed by the solidification front, unless a critical front speed for particle capture is exceeded.[32–39] However, this criterion is not suitable for direct application in continuous casting because the solidification front (1) is dendritic and (2) experiences strong cross flow. The simple capture criterion that particles are entrapped if they touch the solidification front is often used in continuous casting.[13–16,31] This is a reasonable first approximation when the particle diameter is smaller than the Primary Dendrite Arm Spacing (PDAS).[13] When solidification heat transfer and the solid shell are included in the model, simulated particles can be automatically captured when their velocity reaches that of the solid shell.[16,24] However, this method requires a very fine mesh of the mushy region, is very computationally intensive, and needed empirical fitting parameter(s) to match measurements.[16] Yuan, Mahmood, and Thomas[14,15,23] developed a more "advanced" capture criterion, based on a local force balance on the bubble/particle at the solidification front, which includes the effect of particle size, PDAS, interfacial tension, and other effects. This criterion was applied here to study the capture of Ar bubbles in continuous casting process.

Several studies[11,13–17,22,24,30,31] have investigated the capture fraction and distribution of inclusion particles in continuous casting. Early studies of inclusion transport found that large inclusions (>0.64 mm) were likely to be entrapped just below mold,[22,30] while most small particles (<0.04 mm) were trapped deep in the caster.[13,22,30] Large Eddy Simulation (LES) of flow in a thin-slab caster with no argon gas, with the "simple" capture criterion, only 8 pct of all inclusions (<40 μm) were predicted to be removed.[13] The removal fraction was independent of both particle size and density, indicating that the particles were too small to deviate significantly from the flow trajectories of the fluid transporting them.[13] Using a k–ε flow model, including solidification heat transfer and the solid shell, with the simple capture criterion, Wang and Zhang[16] predicted the transport and entrapment of small inclusions in the full length of a billet caster, most 5 μm inclusions were captured deep in the strand. Using flow fields obtained from both RANS and LES simulations, with the advanced capture criterion, Thomas *et al.*[17] investigated the entrapment of larger particles (>40 μm) including slag inclusions, alumina cluster, and bubbles during slab casting, and predicted overall particle removal fraction <20 pct.[17] Gas injection was found to increase the removal rate (average number of inclusions removed per unit time) of small particles.[17] Also, to achieve reproducible results, (removal rate variations within ±3 pct), >2500 particles of each size should be tracked.[17] None of these studies of particle transport included the coupled effects of Ar gas on the flow field.

This paper investigates the transport and capture of argon bubbles in a real commercial continuous caster using both the simple and advanced (force balance criterion[14,15,17]) capture criteria. The results are compared with plant measurements for validation.

II. PLANT MEASUREMENTS

Plant measurements of fluid flow and bubble entrapment were conducted at Baosteel Shanghai in 2012 on the No. 4 continuous slab caster, which casts conventional (230-mm thick) slabs. The flow rate of the molten steel through the SEN into the mold is controlled by a slide gate that moves between the geometric center and the Inside-Radius (IR) side of the caster. For the experiments casting 1300-mm wide slabs at 1.5 m/min, the slide gate was 70 pct open, as shown in Figure 1. Argon gas was injected through porous refractory in the upper tundish nozzle and SEN to prevent clogging, not including Ar gas provided to the slide gate and upper

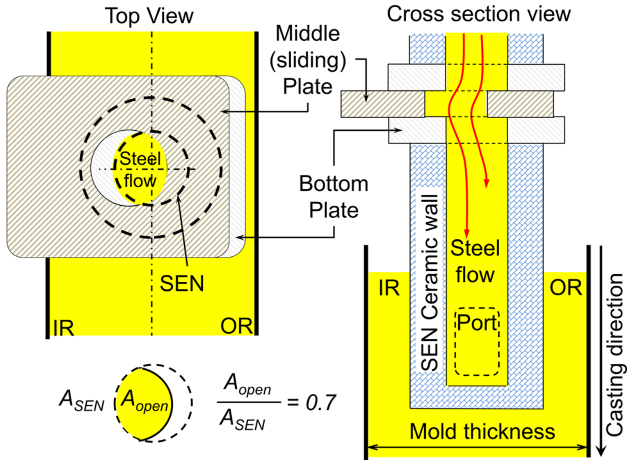

Fig. 1—Slide-gate configuration schematic.

plate seal regions to avoid air aspiration. Top surface velocities were measured with two sets of nailboard dipping tests, which are widely used to measure mold surface flow.[13,40] Specifically, velocities were extracted from the height differences of solidified lumps according to the equation in Figure 4 of Reference 40. Casting conditions and process parameters are given in Table I.

To investigate the capture of Ar bubbles during the process for the same conditions in Table I, samples were cut from the center and quarter of the Wide Face (WF) and Narrow Face (NF) of the steel slab. The sample locations and sizes are shown in Figure 2. To quantify the number and location of the bubbles captured in the samples, the outer 3 mm of the surface of each sample was milled away, and then a ×35 optical microscope was used to record the diameter of each bubble observed on the exposed surface, and the number of bubbles in each size range was counted. After recording the results, another 3 mm steel was milled away and the bubbles on the new exposed surface were measured. This procedure was repeated to examine six layers total, denoted s_j, located at 3, 6, 9, 12, 17, and 22 mm beneath the outer surface of the slab NF or WF. Figure 3 shows a SEM micrograph of a large bubble captured in one of the samples. Note that the many small inclusion particles which cover the surface of the hollowed-out roughly hemispherical depression that comprises most of the bottom half of the original bubble.

Table I. Process Parameters

Process Parameters	Value
Mold thickness (L_t)	230 mm
Mold width (L_w)	1300 mm
SEN submergence depth	160 mm
Nozzle port downward angle	15 deg
Nozzle port area (width × height)	65 × 83 mm^2
Casting speed (V_c)	1.5 m/min
Argon volume fraction (α)	8.2 vol pct
Steel density (ρ)	7000 kg/m^3
Argon density (ρ_p)	0.5 kg/m^3
Steel viscosity (μ)	0.0063 kg/(m s)
Ar viscosity (μ_p)	0.0000212 kg/(m s)
Sample length in casting direction (Δz)	150 mm

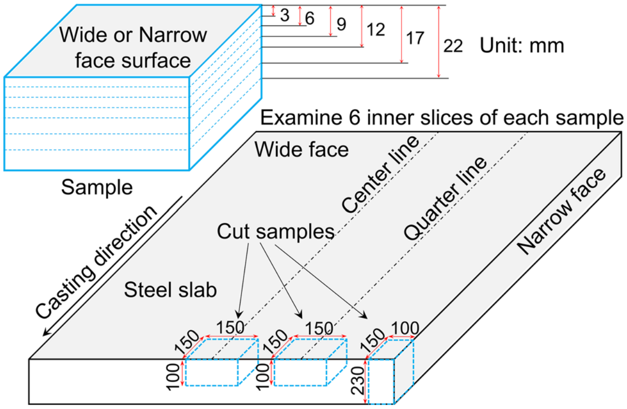

Fig. 2—Locations of samples and six layers examined on each.

III. COMPUTATIONAL MODELS AND SOLUTION PROCEDURE

A three-dimensional finite-volume computational model together with Lagrangian tracking method was applied to study the fully-coupled turbulent flow behavior and the transport phenomena of Ar bubbles in a commercial continuous steel caster. The computational domain includes half of the slide gate, SEN, and mold region (from meniscus surface to 2.5 m below meniscus), as shown in Figure 4. First, steady-state solution of single-phase flow of molten steel was obtained using standard k–ε model. A realistic bubble size distribution was selected and discretized. Then, starting with the single-phase flow field, RANS and Lagrangian DPM coupled simulations were conducted to predict a pseudo-steady flow field solution

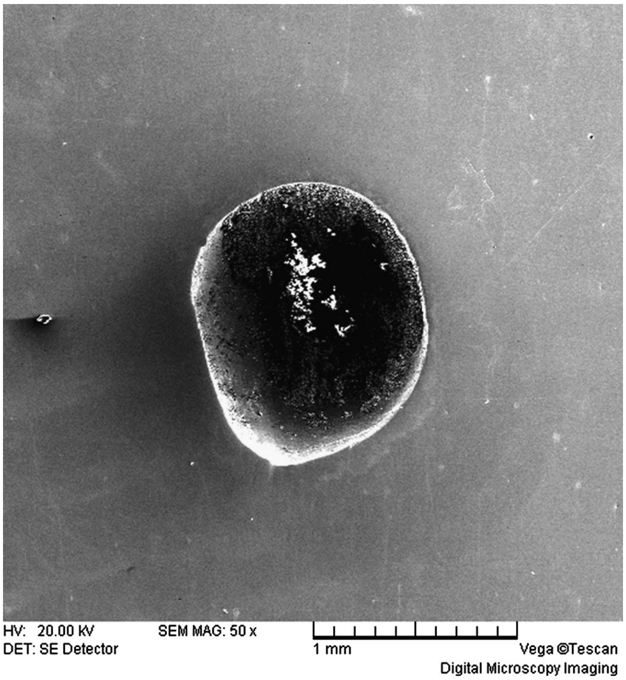

Fig. 3—Example of large bubble (d_p = 1.45 mm) found in plant measurements.

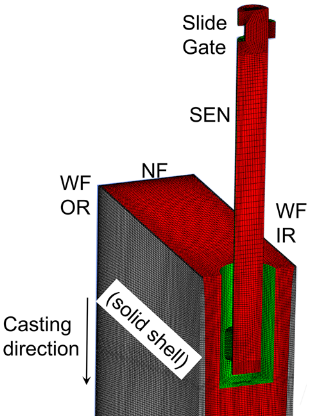

Fig. 4—Mesh of the computational domain of the slide gate, SEN, and mold region.

including the effects of Ar gas injection. The Discrete Random Walk (DRW) model was applied to include the effect of turbulence on bubble dispersion. After that, the flow field was fixed, and ~2.5 million bubbles were injected at the SEN inlet to study the transport phenomena and the capturing of the Ar bubbles. Two different capture models were implemented and compared. The entire solution procedure is shown in Figure 5.

A. *Initial Flow Model*

A single-phase steel flow simulation was first carried out to provide an initial guess for the later two-way coupled steel-Ar flow simulation. Solid shell is included in the domain and the shell thickness can be determined by $s = 3\sqrt{t}$ mm. The solid shell (necessary for later study of magnetic field effects) is modeled as a solid zone in the solver[41] and therefore the fluid flow equations were not solved in the shell region. The continuity and momentum equations for this RANS model are:

$$\frac{\partial}{\partial x_i}(\rho U_i) = S_{\text{mass-sink}}, \qquad [1]$$

$$\rho\frac{\partial U_i}{\partial t} + \rho U_j\frac{\partial U_i}{\partial x_j} = -\frac{\partial p}{\partial x_i} + \frac{\partial}{\partial x_j}\left[(\mu+\mu_t)\left(\frac{\partial U_i}{\partial x_j}+\frac{\partial U_j}{\partial x_i}\right)\right] + S_{i\text{-momentum-sink}}. \qquad [2]$$

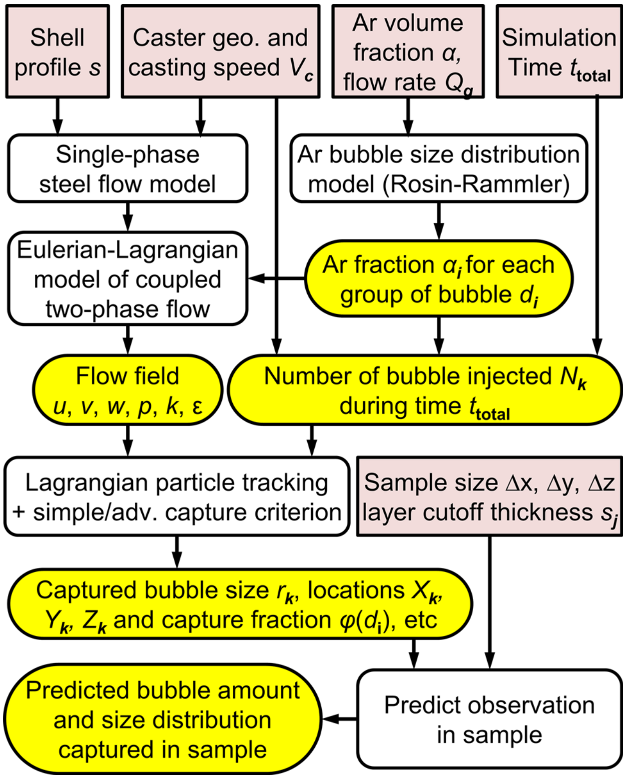

Fig. 5—Flow chart of the entire solution procedure.

Mass and momentum sink (source) terms[14,42,43] were added at cells adjacent to the liquid–solid interface to include the effect of fluid flow across the domain boundary due to solidifying of the shell. The mass sink $S_{\text{mass-sink}}$ is calculated as:

$$S_{\text{mass-sink}} = \rho v_c A_z V_{\text{cell}}^{-1}, \qquad [3]$$

where A_z is the projected shell area of the cell in the casting direction and V_{cell} is the volume of each (red) cell, as illustrated in Figure 6. The momentum sink is the loss of the momentum associated with the mass loss and is evaluated as follows:

$$S_{i\text{-momentum-sink}} = \rho v_c A_z V_{\text{cell}}^{-1} U_i. \qquad [4]$$

The k–ε model was used to model turbulence.[44,45] The turbulent viscosity μ_t needed in Eq. [2], defined as $\mu_t = \rho C_\mu k^2 \varepsilon^{-1}$ is found by solving the following transport equations for k and ε:

$$\frac{\partial}{\partial t}(\rho k) + \frac{\partial}{\partial x_i}(\rho k U_i) = \frac{\partial}{\partial x_j}\left[\left(\mu+\frac{\mu_t}{\sigma_k}\right)\frac{\partial k}{\partial x_j}\right] - \mu_t S^2 - \rho\varepsilon, \qquad [5]$$

$$\frac{\partial}{\partial t}(\rho\varepsilon) + \frac{\partial}{\partial x_i}(\rho\varepsilon U_i) = \frac{\partial}{\partial x_j}\left[\left(\mu+\frac{\mu_t}{\sigma_\varepsilon}\right)\frac{\partial \varepsilon}{\partial x_j}\right] + C_{1\varepsilon}\frac{\varepsilon}{k}\left(\mu_t S^2\right) - C_{2\varepsilon}\rho\frac{\varepsilon^2}{k}, \qquad [6]$$

where $S = \sqrt{2S_{ij}S_{ij}}$ is the modulus of the mean rate-of-strain tensor. The constants in these equations are $C_{1\varepsilon} = 1.44$, $C_{2\varepsilon} = 1.92$, $C_\mu = 0.09$, $C_k = 1.0$, and $C_\varepsilon = 1.3$.

At the slide-gate inlet, fixed velocity $V_{\text{inlet}} = 1.69$ m/s was applied, based on steel volume flow rate (0.007475 m^3/s) divided by inlet area (0.0044 m^2). The turbulent kinetic energy and its dissipation rate were assumed to be small as 10^{-4} m^2/s^2 and 10^{-5} m^2/s^3, respectively. A pressure outlet boundary condition was applied at the domain bottom based on the ferrostatic pressure of steel (171.5 kPa) at that distance (2.5 m below the top surface) multiplied by the steel density and gravity constant. The turbulent kinetic energy and its dissipation rate were specified as 10^{-5} m^2/s^2 and 10^{-5} m^2/s^3 for reverse flow from the bottom boundary, respectively. A free slip boundary condition was applied at the top

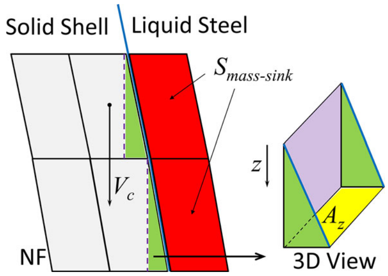

Fig. 6—Computation of mass sink term for shell solidification.

surface of the mold. The WF and NF solidification fronts and SEN walls had standard wall laws.[45]

B. *Bubble Size Distribution Model*

In this study, the Ar gas volume was distributed into bubbles according to a Rosin–Rammler[34] size distribution, which was originally used to describe solid particle distributions. The ideal Rosin–Rammler cumulative distribution $F(d)$ is defined by the mean diameter d_{mean} and spread parameter η

$$F(d_i) = \frac{V_{\mathrm{g}(d<d_i)}}{V_{\mathrm{g}}} = 1 - \exp\left(-\frac{d_i}{d_{\text{mean}}}\right)^{\eta}. \qquad [7]$$

In this work, a discrete form of this distribution function was based on 11 different bubble sizes, d_i, where i is the bubble size group, and $F(d_i)$ is the volume fraction of Ar contained in those bubbles with diameter less than d_{i}.

The average bubble diameter d_{mean} was taken as 3 mm, based on calculations with a previously validated two-stage model of Ar injection into downward flowing steel[2,28] for the flow rates used in this work. This value also matches recent work[21] based on water model measurements using a MuSiG model. The spread parameter η was taken as 4, based on a measurement in a water model[46] and adjusted to account for increased surface tension in steel/argon using a relation from previous measurements[2,28] and recent measurements[47] of bubble distributions.

The volume fractions of bubbles with different diameters are given in Figure 7, where different definitions of the mean bubble diameters are noted. The blue squares represent the diameter and volume fraction of each group of bubbles of the total Ar volume used in the model. The red staircase-like line is the summation over the volume fraction of bubbles with diameter less than the specified diameter. This staircase Rosin–Rammler cumulative distribution is compared with the ideal distribution, plotted as a dashed line, which overlaps at discrete points. Note also that bubbles smaller than 1 mm in diameter comprise less than 1 pct of the total bubble volume.

C. *Two-Phase Flow Model*

After the single-phase fluid flow solution was obtained, the effect of the Ar gas bubbles on fluid flow was added. The Eulerian k–ε flow model with Lagrangian DPM tracking and DRW model was used to include this phenomenon. In this two-way coupled Eulerian-DPM model, an additional source term $\boldsymbol{S}_{\text{DPM}}$ is added to Eq. [2], to include the net force from the Ar bubbles to the local fluid. The following force balance equation was solved for each individual bubble with mass m_{p} and velocity $\boldsymbol{u}_{\mathrm{p}}$:

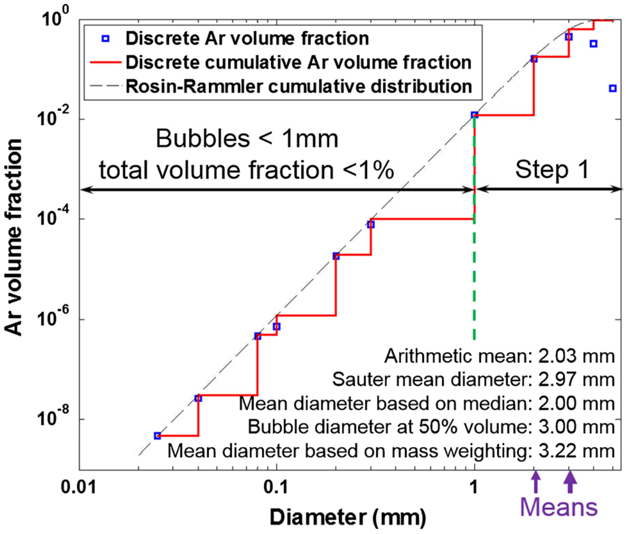

Fig. 7—Ar bubble volume fraction distribution.

$$m_{\mathrm{p}} \frac{\mathrm{d}\boldsymbol{u}_{\mathrm{p}}}{\mathrm{d}t} = \underbrace{\frac{m_{\mathrm{p}} 18\mu}{\rho_{\mathrm{p}} d_{\mathrm{p}}^2}\frac{C_{\mathrm{D}}}{24}(\boldsymbol{u}-\boldsymbol{u}_{\mathrm{p}})\overbrace{\frac{\rho d_{\mathrm{p}}|\boldsymbol{u}_{\mathrm{p}}-\boldsymbol{u}|}{\mu}}^{\mathrm{Re}_{\mathrm{p}}}}_{\boldsymbol{F}_D} + \underbrace{0.5 m_{\mathrm{p}} \frac{\rho}{\rho_{\mathrm{p}}}\left(\frac{\mathrm{D}\boldsymbol{u}}{\mathrm{D}t}-\frac{\mathrm{d}\boldsymbol{u}_{\mathrm{p}}}{\mathrm{d}t}\right)}_{\boldsymbol{F}_{\mathrm{v}}} + \underbrace{m_{\mathrm{p}}\frac{\rho}{\rho_{\mathrm{p}}}\frac{\mathrm{D}\boldsymbol{u}_{\mathrm{p}}}{\mathrm{D}t}}_{\boldsymbol{F}_{\mathrm{p}}} + \underbrace{m_{\mathrm{p}}\frac{\boldsymbol{g}(\rho_{\mathrm{p}}-\rho)}{\rho_{\mathrm{p}}}}_{\boldsymbol{F}_{\mathrm{b}}}, \qquad [8]$$

where the four forces are: drag $\mathbf{F}_{\mathrm{D}}$, virtual mass $\mathbf{F}_{\mathrm{V}}$, pressure gradient effect $\mathbf{F}_{\mathrm{p}}$, and buoyancy/gravity $\mathbf{F}_{\mathrm{b}}$. The drag force depends on particle Reynolds number Re_{p} and the drag coefficient C_{D} was computed based on the drag law proposed by Morsi *et al.*[48]:

$$C_{\mathrm{D}} = a_1 + \frac{a_2}{Re_{\mathrm{p}}} + \frac{a_3}{Re_{\mathrm{p}}^2}, \qquad [9]$$

$$a_1, a_2, a_3 = \begin{cases} 0, 24, 0 & \\ 3.690, 22.73, 0.0903 & 0.1 < Re_{\mathrm{p}} < 1 \\ 1.222, 29.1667, -3.8889 & 1 < Re_{\mathrm{p}} < 10 \\ 0.6167, 46.50, -116.67 & 10 < Re_{\mathrm{p}} < 100 \\ 0.3644, 98.33, -2778 & 100 < Re_{\mathrm{p}} < 1000 \\ 0.357, 148.62, -47500 & 1000 < Re_{\mathrm{p}} < 5000 \\ 0.46, -490.546, 578700 & 5000 < Re_{\mathrm{p}} < 10000 \\ 0.5191, -1662.5, 5416700 & Re_{\mathrm{p}} > 10000 \end{cases} \qquad [10]$$

The first 3 of these forces comprise $\mathbf{S}_{\mathrm{DPM}}$. To save computation time and considering that the volume fraction $d_{\mathrm{p}} < 1$ mm bubbles is so small, the effect of these small bubbles on the mold flow pattern in this two-way coupled simulation was negligible. Therefore, only the large bubbles (1 to 5 mm) were injected and tracked in this step.

To include the effect of turbulence on particle dispersion, a DRW model was used,

$$u_i = U_i + u_i' \approx U_i + \zeta\sqrt{2k/3}, \tag{11}$$

where the local fluid velocity u_{i} is a function of local time averaged velocity U_{i}, local turbulent kinetic energy k, and a normally-distributed random number ζ with mean 0 and standard deviation 1. During the calculation, ζ changes to produce a new instantaneous velocity fluctuation whenever the time reaches the smaller of: the eddy lifetime t_{e} and the time needed to cross the eddy t_{cross}, which are defined as follows:

$$t_{\mathrm{e}} = -0.15\frac{k}{\varepsilon}\ln(\gamma), \tag{12}$$

$$t_{\mathrm{cross}} = -\tau_{\mathrm{p}}\ln\left[1 - \frac{C_{\mu}^{4/3}\,\frac{k^{3/2}}{\varepsilon}}{\tau_{\mathrm{p}}\left|\boldsymbol{u} - \boldsymbol{u}_{\mathrm{p}}\right|}\right] \quad \text{where} \quad \tau_{\mathrm{p}} = \frac{\rho_{\mathrm{p}} d_{\mathrm{p}}^2}{18\mu}, \tag{13}$$

where γ is a random number uniformly distributed from 0 to 1, and τ_{p} is the particle relaxation time which represents a time scale for a particle to respond to changes in the surrounding flow. The velocity and position of each particle is computed and updated until it escapes or is captured.

D. *Bubble Tracking and Capture Model*

After solving for the steady-state flow fluid using the Eulerian–Lagrangian model, particles were injected into the domain and their trajectories were tracked. The number of bubbles injected with diameter d_i, denoted $N(d_i)$, is determined to match the plant experiment conditions as follows:

$$N(d_i) = \frac{3\alpha_i}{4\pi(0.5d_i)^3} \cdot \underbrace{\alpha\frac{t_{\mathrm{total}} V_{\mathrm{c}} L_t(0.5L_{\mathrm{w}})}{1-\alpha}}_{V_{\mathrm{g}}} \tag{14}$$

$$\text{where} \quad \alpha_i = \begin{cases} F(d_i) & i = 1 \\ F(d_i) - F(d_{i-1}) & i > 1 \end{cases}$$

where V_{g} is the volume of total Ar gas injected into half of the caster during the chosen time t_{total} of 60 seconds; L_{t} and L_{w} are the strand thickness and width, respectively; and α is the total Ar volume fraction of 8.2 pct. The volume fractions for bubbles of different sizes are denoted as α_i, and can be determined based on $F(d_{\mathrm{i}})$ from Eq. [5]. Following these equations, ~2.5 million bubbles were injected over 60 seconds and tracked for each capture criterion.

Two different capture criterion were implemented in this work: (1) a "simple" capture criterion which assumes immediate capture when a bubble/particle touches the solidification front; (2) an "advanced" capture criterion that based on the force balance proposed by Yuan and Thomas.[14,15,23] The flow chart in Figure 8 shows the procedure of this advanced capture criterion. For small bubbles less than the PDAS, the particle can enter between the dendrite arms and be captured by entrapment. For bubbles/particles greater than the PDAS, the advanced criterion considers eight forces acting on a spherical bubble/particle touching three dendrite arms, shown in Figure 9. In addition to the four forces shown in Eq. [6], lift force F_{L}, lubrication force F_{lub}, Van der Waals force F_{IV}, and surface tension gradient force F_{Grad} were also considered[14,15,17,23]:

$$F_{\mathrm{L}} = -\frac{9}{4\pi}\mu d_{\mathrm{p}}^2 U_{\mathrm{s}}\,\mathrm{sgn}(G)\left[\frac{|G|}{v}\right]^{1/2} J, \quad G = \frac{\mathrm{d}u_1}{\mathrm{d}y},$$
$$\varepsilon = \mathrm{sgn}(G)\frac{\sqrt{v|G|}}{U_{\mathrm{s}}}, \quad U_{\mathrm{s}} = u_1 - v_1 \tag{15}$$
$$J(\varepsilon) = 0.6765[1 + \tanh(2.5\log_{10}\varepsilon + 0.191)][0.667 + \tanh(6\varepsilon - 1.92)]$$

$$F_{\mathrm{lub}} = 6\pi\mu V_{\mathrm{sol}}\frac{R_{\mathrm{p}}^2}{h_{\mathrm{o}}}\left(\frac{r_{\mathrm{d}}}{r_{\mathrm{d}} + R_{\mathrm{p}}}\right)^2 \tag{16}$$

$$F_{\mathrm{IV}} = 2\pi\left(E_{\mathrm{sp}} - E_{\mathrm{sl}} - E_{\mathrm{pl}}\right)\frac{r_{\mathrm{d}} R_{\mathrm{p}}}{r_{\mathrm{d}} + R_{\mathrm{p}}}\frac{a_{\mathrm{o}}^2}{h_{\mathrm{o}}^2} \tag{17}$$

$$F_{\mathrm{Grad}} = -\frac{m\beta\pi R_{\mathrm{p}}}{\xi^2}\left\{\frac{\xi^2 - R_{\mathrm{p}}^2}{\beta}\ln\frac{(\xi + R_{\mathrm{p}})\left[\alpha(\xi - R_{\mathrm{p}}) + \beta\right]}{(\xi - R_{\mathrm{p}})\left[\alpha(\xi + R_{\mathrm{p}}) + \beta\right]}\right\}$$
$$+\frac{2R_{\mathrm{p}}}{\alpha} - \frac{\beta}{\alpha^2}\ln\frac{\alpha(\xi - R_{\mathrm{p}}) + \beta}{\alpha(\xi + R_{\mathrm{p}}) + \beta}, \tag{18}$$

where u_1 and v_1 are instantaneous streamwise velocities for the liquid and particle; R_{p} is the radius of the particle; r_{d} is the radius of the dendrite tip; h_0 is the distance between the particle and the dendrite tip; a_0 is the atomic diameter of liquid steel; E is the surface energy and the subscripts s, p, and l denote the solid steel, particle/bubble, and liquid steel respectively; $\xi = R_{\mathrm{p}} + r_{\mathrm{d}} + h_0$, $\alpha = 1 + nC_0$, and $\beta = (C^* - C_0)nr_{\mathrm{d}}$ where m, n, C^*, and C_0 are model parameters. More details about the formulation of these forces can be found in previous work.[14,15,23] Note that bubbles reaching the bottom of the domain were also considered as captured.

The captured bubbles were then analyzed to compute the capture rate and capture fraction for difference size of bubbles for both capture criteria. The captured

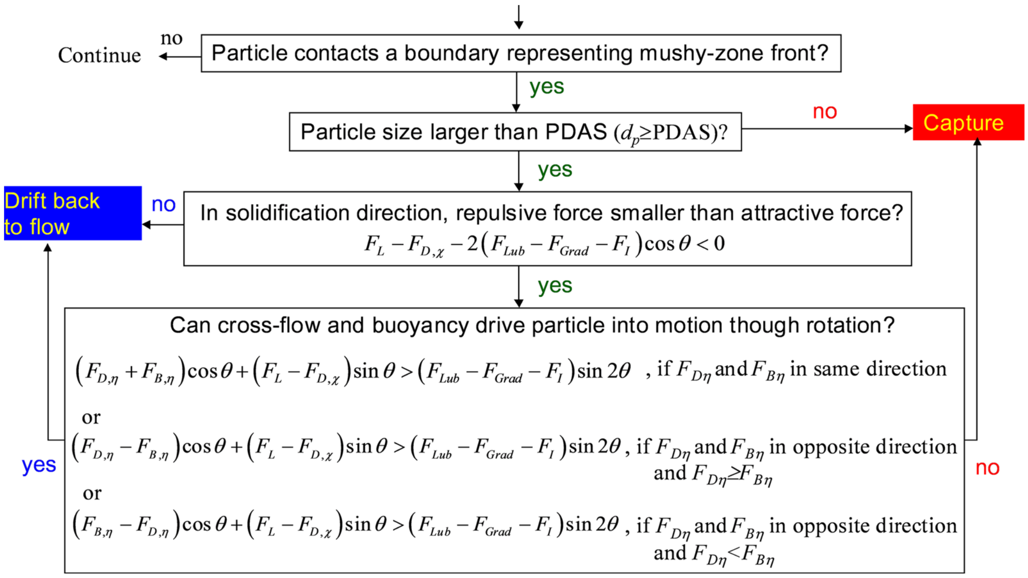

Fig. 8—Flow chart for Ar bubble/particle capture criterion.[17]

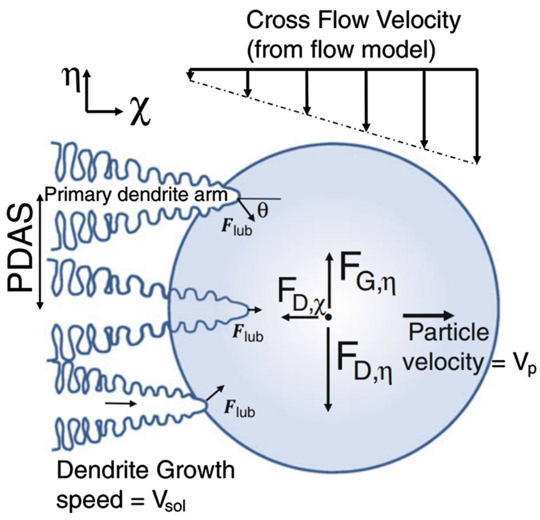

Fig. 9—A bubble/particle touching 3 dendrite tips [17].

numbers of bubbles and their diameters were recorded, and the capture fractions for bubbles of different diameters were denoted as φ calculated using:

$$\varphi(d_i) = \frac{n(d_i)}{N(d_i)}, \qquad [19]$$

where, $n(d_i)$ denotes the capture rate, or number of captured bubbles of diameter d_i in the entire caster during a chosen time interval.

E. *Model to Predict Sample Observations*

To compare with plant measurements, the first step is to determine the number $n_{\text{sample}}(d_i)$ of each bubble size captured during the time the samples were cast, which is determined as follows:

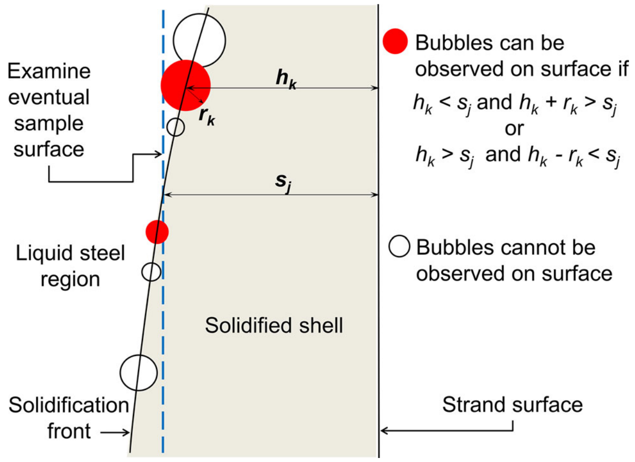

Fig. 10—Determine the number of bubbles can be observed on surface.

$$n_{\text{sample}}(d_i) = n(d_i)\frac{t_{\text{total}}}{t_{\text{sample}}}, \qquad [20]$$

where t_{total} is 60 seconds in this study and $t_{\text{sample}} = V_c/\Delta z$, is 6 seconds in this study.

Next, the bubbles that can be observed on each sample surface must be extracted from these results. As illustrated in Figure 10, a bubble k with radius r_k captured at a distance h_k beneath the strand surface, can be observed on surface j located at distance s_j beneath the outer slab surface (WF/NF) only if it satisfies one of the following conditions:

$$\{h_k < s_j \text{ and } h_k + r_k > s_j\} \quad \text{or} \quad \{h_k > s_j \text{ and } h_k - r_k < s_j\}. \qquad [21]$$

These conditions were checked for each bubble to extract the number and average diameter of bubbles predicted to be observed on each examined sample layer.

The polished sample surface is unlikely to cut through captured bubbles at their largest center diameter. Thus, the observed circle diameters are usually smaller than the real sphere diameters, as illustrated in Figure 11. A simple method proposed by Lekakh *et al.*[49] was used here to convert the observed diameters into realistic diameters of the spherical bubbles, which are presented in the results

$$d_{\text{true}} = d_{\text{visible}}/0.785. \qquad [22]$$

F. *Computational Details*

The above models were implemented into the commercial finite-volume package ANSYS FLUENT[41] and solved on the structured mesh of ~1 million hexahedral cells shown in Figure 4, according to the flow chart in Figure 5. The mass and momentum sinks and the advanced capture criterion were added through a User Defined Function (UDF). The simulations were run in parallel on a six-processor Intel Xeon X5650 CPU (2.66GHz). First, the single-phase model was run for the initial condition, which took ~1 day of CPU time. Then, about 3 days were needed for the two-phase fluid flow solution. Then, about 1 day CPU time was needed to track the ~2.5 million bubbles for each capture criterion. Finally, a MATLAB code was used to process the output data to extract the predicted distributions in the sample, which took ~3 hours to run.

IV. MODEL RESULTS AND DISCUSSION

A. *Fluid Flow in SEN and Mold*

Contours of steel flow speed and velocity vectors on the symmetry plane of the SEN and slide gate are shown in Figure 12. Because the slide gate moves toward the IR, the steel flow down that side of the SEN is stronger. This leads to a counter-clockwise eddy or "swirl" at the SEN bottom region. This swirl extends completely through the port as shown in Figure 13. Consequently, a higher Ar volume fraction region (gas pocket) is seen at the top and IR side of the port, where more Ar bubbles escape. This gas pocket matches observations in water models, although the calculation is not exact, owing to local mass imbalance inherent to the computational method in regions of high gas fraction.

Contours of steel velocity magnitude and streamlines in the middle plane of the caster mold are shown in Figure 14. The standard double-roll flow pattern is

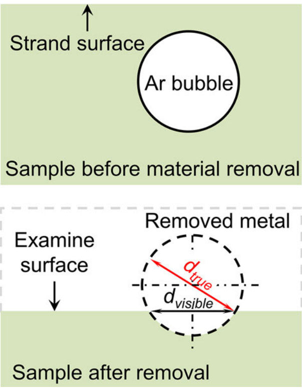

Fig. 11—Convert hole diameter observed on sample surface to true bubble diameter.

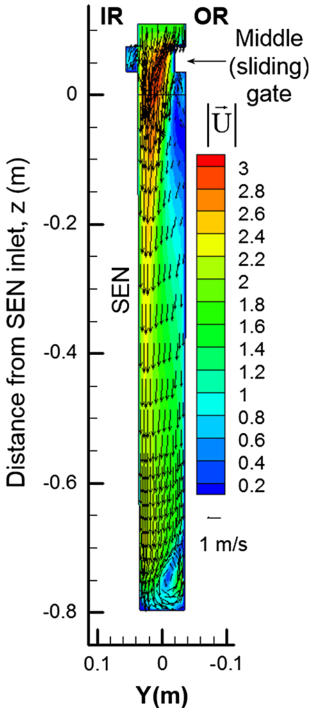

Fig. 12—Ar volume fraction and velocity field in symmetry plane of SEN.

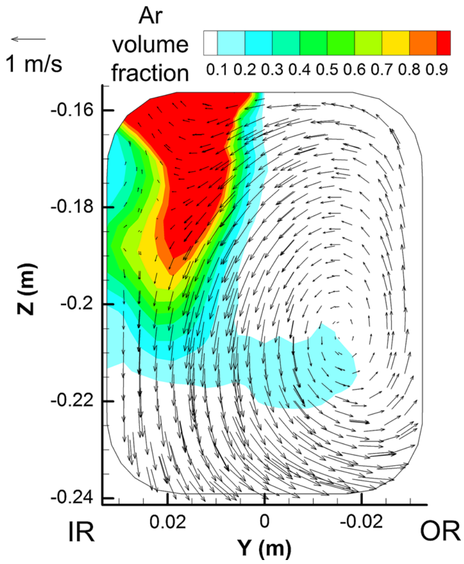

Fig. 13—Ar volume fraction and steel vector field at port outlet.

modified by the Ar injection and three eddies (recirculation regions) were observed (labeled 1, 2, 3). The nozzle jets impinge on the narrow face and split, sending some recirculating flow upwards and across the top surface toward the SEN. This is met by flow rising up beside the SEN driven by the buoyancy of the Ar gas. The asymmetric swirl caused by the slide gate sends more gas up the inner radius (IR) of the WF.

Contours of Ar volume fraction and steel velocity vectors at 1 cm below the top surface are shown in Figure 15. The surface flow pattern is separated into two zones by the purple dashed line. Surface flow near the SEN is driven by eddy 2 in Figure 14 and is caused by the high buoyancy of the flow containing high Ar gas fraction. The opposite flow from the NF is driven by eddy 3 in Figure 14 from flow up the NF wall. The upward flow near the SEN is biased toward the IR side of the mold wall, due to the port swirl caused by the slide-gate movement toward the IR. This Ar-rich flow upwells on the top surface from the IR, causing strong cross flow across most of the top surface toward the OR. The maximum cross flow velocity reaches ~0.3 m/s.

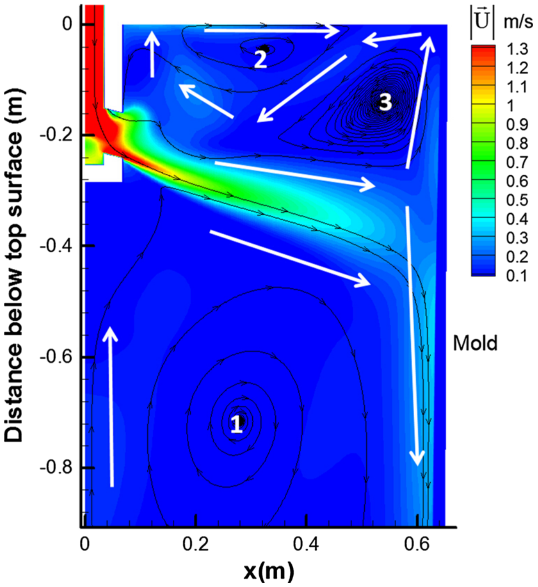

Fig. 14—Velocity magnitude and streamlines in middle plane.

It also important to mention that this biased flow is not seen in the single-phase simulation step. Therefore, this biased flow pattern is induced by the combined effect of asymmetric slide-gate movement and the Ar gas injection. Without Ar gas, the asymmetric effect caused by the slide gate is only important in the SEN and the swirl exiting the ports dissipates in the mold. With enough Ar injection, the slide-gate movement causes the important effect of detrimental asymmetric cross flow on the top surface.

B. *Bubble Capture Locations*

The trajectories and capture locations of 2.5 million Ar bubbles of different sizes were calculated based on the steady-state flow solution, for both the simple and advanced capture criteria. The captured locations of the small ($d_p < 0.1$ mm) and medium-sized ($0.1 \le d_p \le 0.3$ mm) bubbles are shown in Figures 16 and 17, for the simple and advance capture criterion, respectively. The horizontal black lines show the location of the sample surfaces examined in the measurements.

All figures show that the number of bubbles captured by the solidifying shell decreases with distance down the caster. However, many small bubbles are captured deep in the caster, which agrees with previous studies.[16,22,29,30] More bubbles are captured near the SEN on the IR WF, but on the OR WF more bubbles are captured near the narrow face, especially where the jet spreads to impinge on the solidification front. Many bubbles are captured on the narrow face in the mold near and above the point of jet impingement. Comparing Figures 16 and 17 shows that 1.4× fewer 0.3 mm bubbles (red dots) were captured when using the advanced capture criterion.

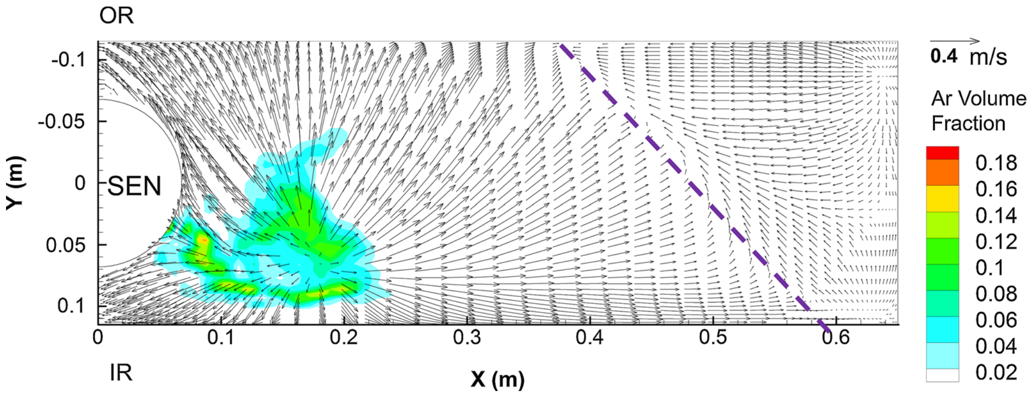

Fig. 15—Velocity and Ar volume fraction near top surface.

Large captured bubbles ($d_p \ge 1$ mm) are most detrimental to the final product. With the simple criterion, Figure 18 shows many large bubbles captured on the solidifying walls, especially on the IR, where many captured bubbles exceeded 3 mm. Elsewhere, on OR and NF, the captured large bubbles were mainly ≤1 mm. With the advanced capture criterion, Figure 19 shows that relatively few large bubbles (≤2 mm) were captured

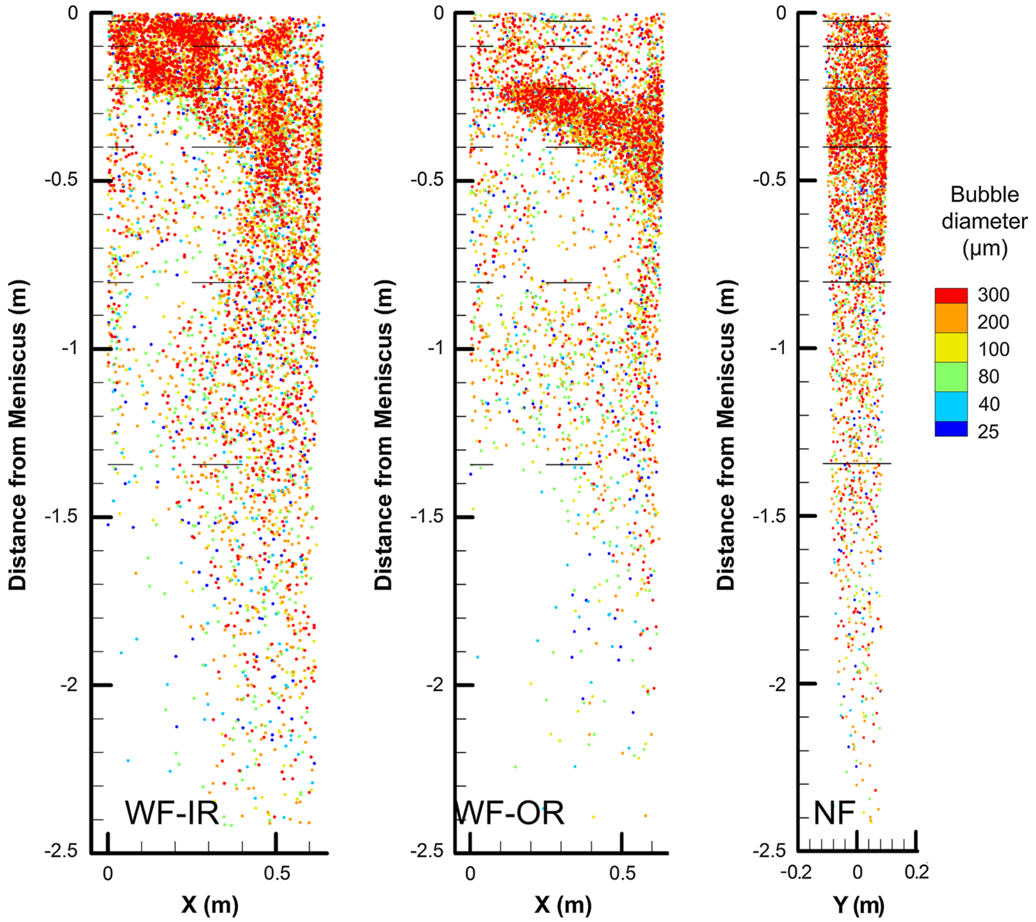

Fig. 16—Small bubbles captured by WF-IR (left), WF-OR (middle) and NF (right) using simple capture criterion.

and mostly very close to the meniscus, which agrees with previous results.[22,29,30]

The locations where argon bubbles escaped from the top surface are plotted in Figure 20. As expected, most large bubbles escape near the SEN, biased toward the IR side of the caster, where the gas fraction was highest in Figure 15. Figure 20 also shows that smaller bubbles are more evenly distributed over the surface. Relatively few small bubbles ($d_p < 0.1$ mm) are seen escaping the top surface, which indicates that most small bubbles are captured in the cast product.

C. *Bubble Capture Rate and fraction*

Figure 21 shows the capture rates of different Ar bubble sizes, comparing the simple and advanced capture criteria. The total injection rate of each bubble size is plotted with an open circle. To compare with the measurements, the capture rates were evaluated for 6 seconds (the time to cast the sample length $\Delta z = 150$ mm) and summed over the entire caster. The predicted capture rates for bubbles less than 0.2 mm by the simple and advanced capture criteria are very close and were only slightly lower than the injection rate.

In contrast, huge differences in capture rates were observed for larger bubbles. The simple criterion predicted round 3000 1 mm bubbles captured in the entire caster during 6 seconds of casting process, while the advanced capture criterion predicted around 50 bubbles per 6 seconds, which is 60× fewer. With larger bubbles, the advanced criterion predicted even fewer (up to 500× fewer). The capture rate dropped rapidly with increasing bubble diameter for both capture criteria.

It important to note that no bubbles greater than 3 mm diameter were captured when using advanced capture criterion or in the measurements. In the plant measurements, only one 1.4 mm bubble was observed in one of the examined layers. To compare with the model predictions, the measurements were scaled based on the peripheral of the caster. Specifically, only one 1.4 mm bubble was observed in one of the examined layers of all of the sample layers, which extended 530 (150 + 150 + 230) mm of the total 3060 (1300 + 1300 + 230 + 230) mm perimeter. This means that around 6 captured bubbles would be expected if the entire perimeter were examined, which is the number plotted as the scaled experiment. Note that even more than 6 bubbles should be found if the experiments examined the entire samples instead of only 6 slices. Considering this would increase the measurements closer to the 40 ~1 mm bubbles predicted by the advanced criterion.

The fraction of bubbles that are captured is plotted in Figure 22 for different sizes. The capture fractions of small bubbles (any $d_p < 0.1$ mm) is ~0.85 for both

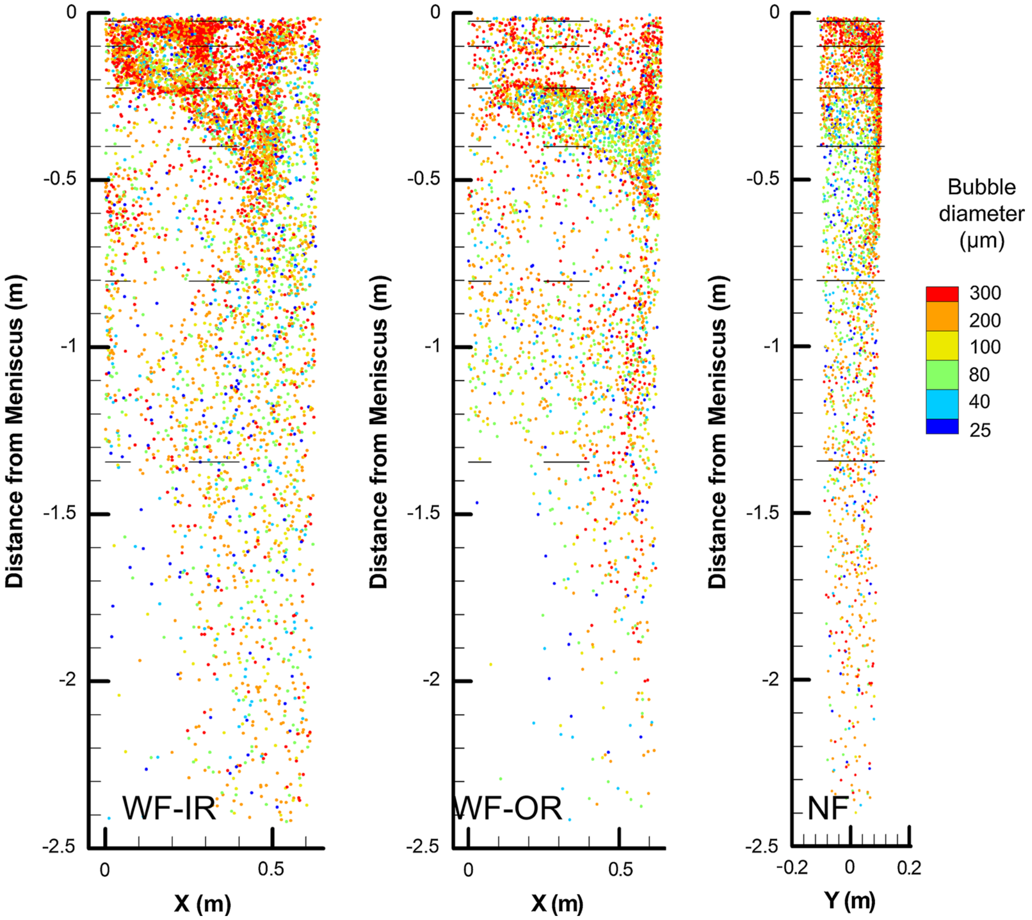

Fig. 17—Small bubbles captured by WF-IR (left), WF-OR (middle), and NF (right) using advanced capture criterion.

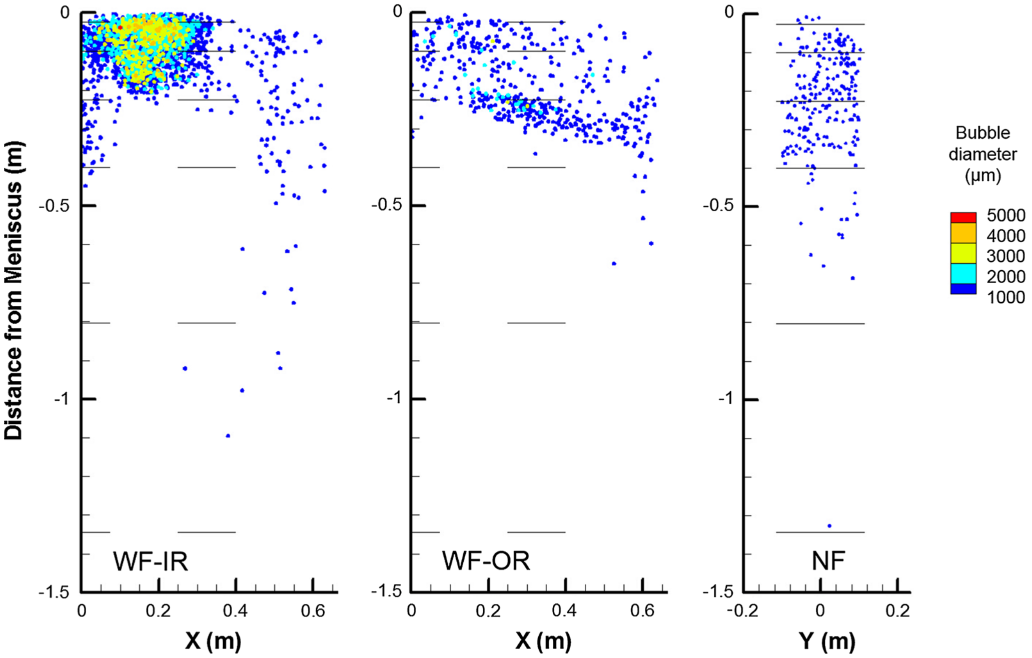

Fig. 18—Large bubbles ($d_p \geq 1$ mm) captured by WF-IR (left), WF-OR (middle), and NF (right) using simple capture criterion.

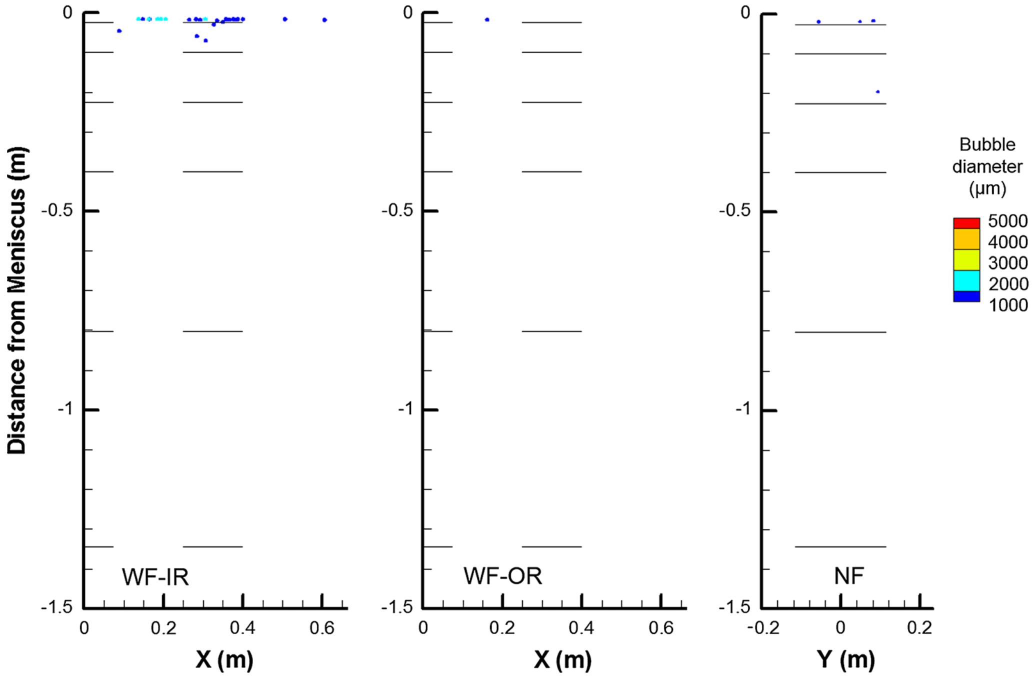

Fig. 19—Large bubbles ($d_p \geq 1$ mm) captured by WF-IR (left), WF-OR (middle), and NF (right) using advanced capture criterion.

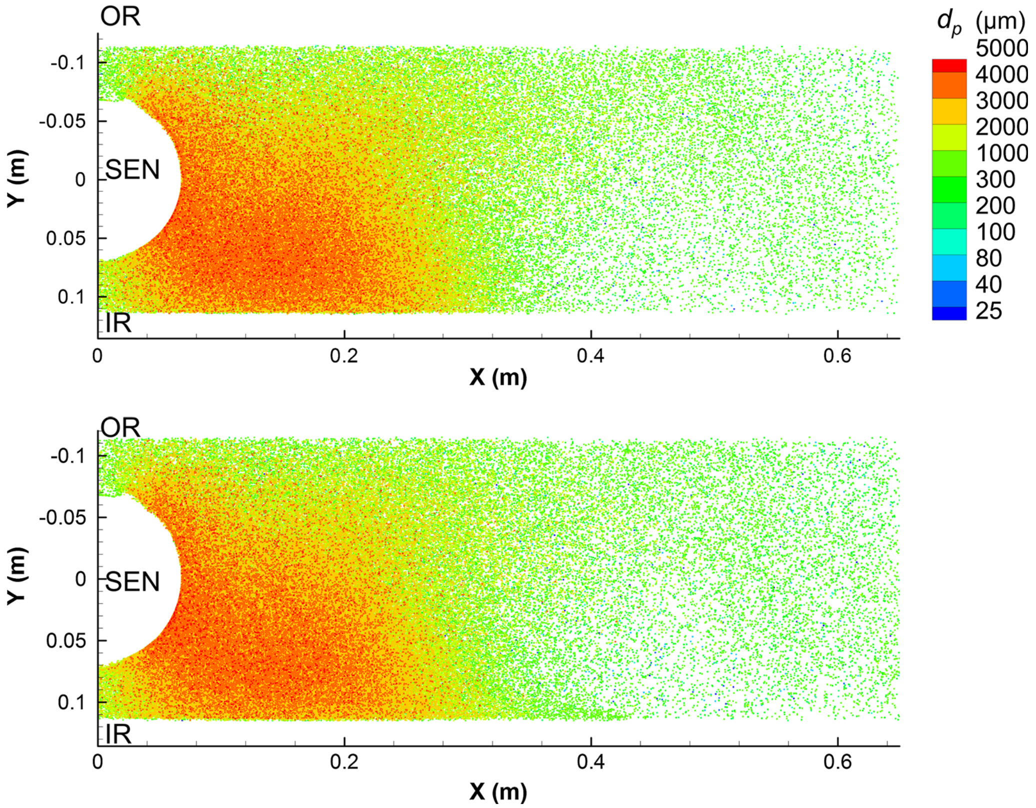

Fig. 20—Bubbles escaped from top surface using simple (top) and advanced (bottom) capture criterion.

capture criteria. The uniformity of this value for any small size shows that the capture fraction of bubbles smaller the PDAS is governed only by the flow pattern. However, the capture fractions of large bubbles decreases dramatically with increasing bubble size. The capture fraction of 1 mm bubbles was 6 pct with the

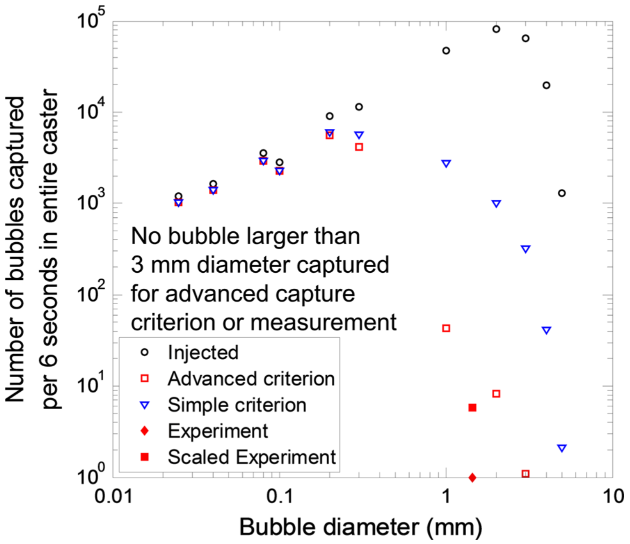

Fig. 21—Number of bubbles captured per 6 seconds in entire caster.

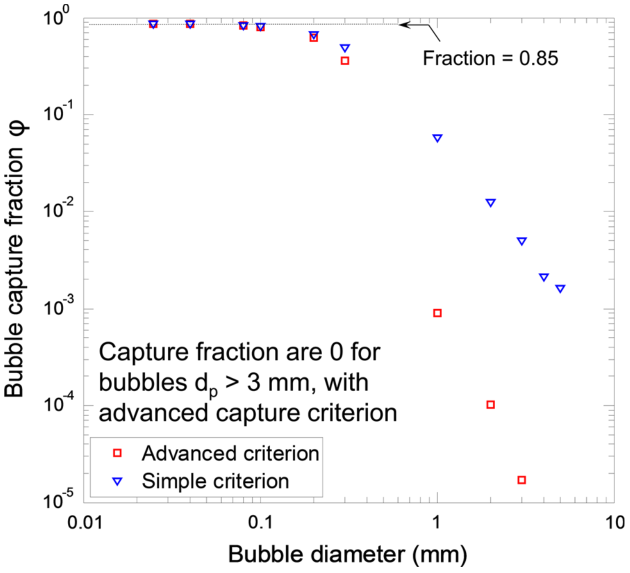

Fig. 22—Bubble capture fraction for different bubble diameters.

simple capture criteria but only 0.1 pct with the advanced capture criterion. The advanced criterion predicts a drop of about one order of magnitude in capture fraction from 0.01 pct of 1 mm bubbles to 0.01 pct of 2 mm bubbles, to 0.001 pct of 3 mm bubbles, and no capture at all of bubbles larger than 3 mm.

D. *Bubble Removal Fraction and Capture Distribution with Advanced Criterion*

The removal fraction for different bubbles and the relation between bubble capture percentages and distance below meniscus are illustrated in Figure 23. The removal fraction for large bubbles ($1 \leq d_p \leq 5$ mm) was 99.98 pct, for medium bubbles ($0.1 \leq d_p \leq 0.3$ mm) was ~48.5 pct, and for small bubbles ($d_p < 0.1$ mm) was ~16.1 pct. Previous RANS and LES studies[9] showed removal rates for 0.1 and 0.4 mm slag particles of ~13 and ~47 pct, which is close to the present results. These Sankey diagrams also reveal that large bubbles are very rarely captured in the casting process. Around 39 pct of small bubbles and 28 pct of medium bubbles are captured within 0.5 m of the meniscus, which is confined to the first 13 mm of shell growth in the current study. The trend of less capture with downward distance in the casting direction is also illustrated. This means less bubbles would be captured in the interior region of the slab. Below 0.5 m, the capture fraction of medium bubbles decreases to about half that of small bubbles. The average capture percentage for large bubbles was around 0.02 pct which is very small, and they are only be captured at the top region of the meniscus, which means very close to the strand surface.

The capture rates of different size ranges of bubbles at different locations are illustrated in Figure 24. Capture rates were calculated from the number of bubbles captured within a region (labeled from I to IV in Figure 24) divided by the casting time (6 seconds in this case) and the surface area of the region. Capture rates decrease with distance below the meniscus. The capture rates of medium bubbles were larger than both small and large bubbles in each region. Capture rates on the IR side were larger than on the OR side. This is due to more gas flow leaving the port toward the IR side, increasing bubble volume fraction near the IR.

The measured number of bubbles captured per cm^2 at different depths beneath the WF/NF are compared in Figure 25 with predictions using the advanced criterion. In the center region, Figure 25(a) shows that the predicted 0.05 to 0.1 bubbles/cm^2 captured is close to the measurements of 0.05 to 0.2 bubbles/cm^2. The predictions match better deeper beneath the strand surface, but under-predict capture significantly near the meniscus. This may be due to the neglect of hook capture mechanism in the current model. Meniscus solidification creates hooks which extend out from the solidification front and entrap rising bubbles into the shell. This mechanism occurs only near the meniscus before hooks are overtaken by the growing shell and no longer affect capture. At the quarter regions, Figure 25(b) shows that more bubbles were predicted to be captured per cm^2 on the OR than the IR. The OR predictions matched better with the measurements. On the NF, Figure 25(c) shows that the predicted 0.05 to 0.13 bubbles/cm^2 captured are close to the measurements of 0 to 0.17 bubbles/cm^2. Fewer bubbles are captured deeper in the slab.

V. MODEL VALIDATION

The results of this work show reasonable agreement between the computational model predictions and the measurements.

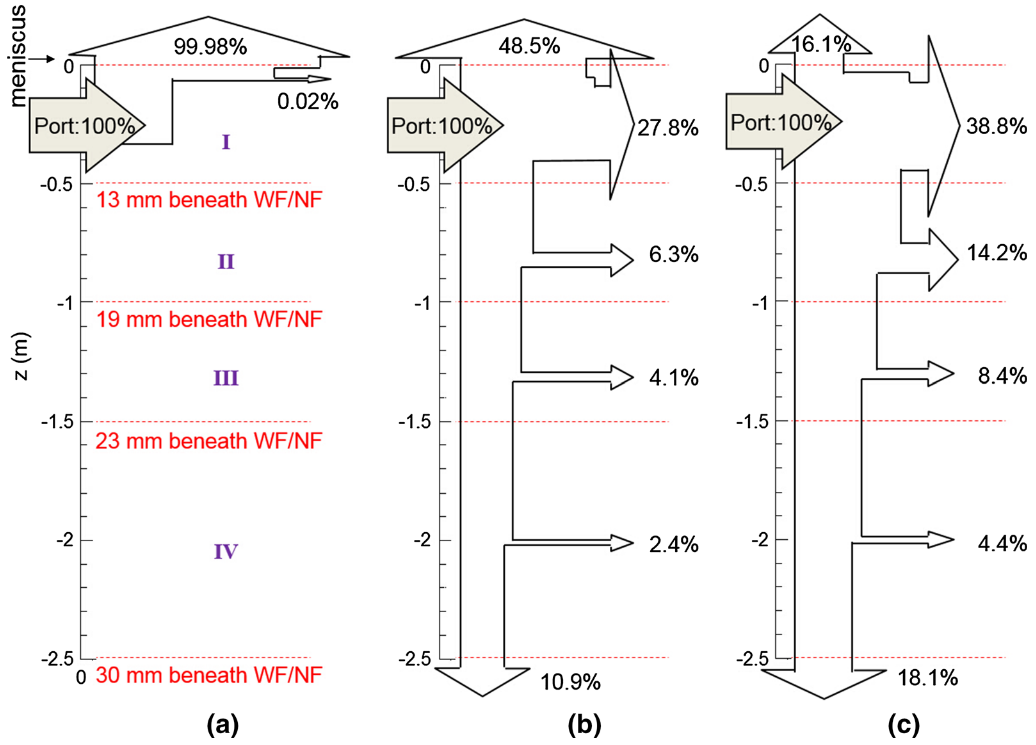

Fig. 23—Sankey diagram of number of bubbles captured in different zones for (*a*) large bubbles, (*b*) medium bubbles, and (*c*) small bubbles.

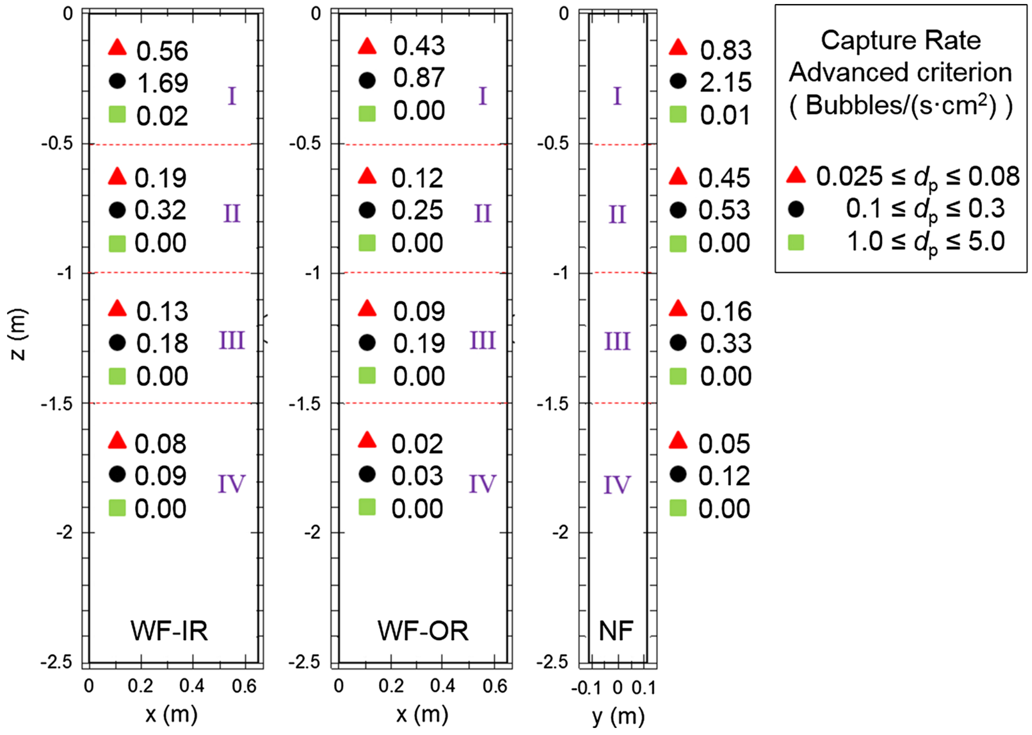

Fig. 24—Capture rate for small, medium, and large bubbles in different zones.

A. *Surface Velocities*

The speed profile across and just beneath the top surface centerline from the multiphase flow model are compared with the plant nailboard measurements in Figure 26. The strong cross flow predicted from IR toward OR agrees with plant measurements. The cross

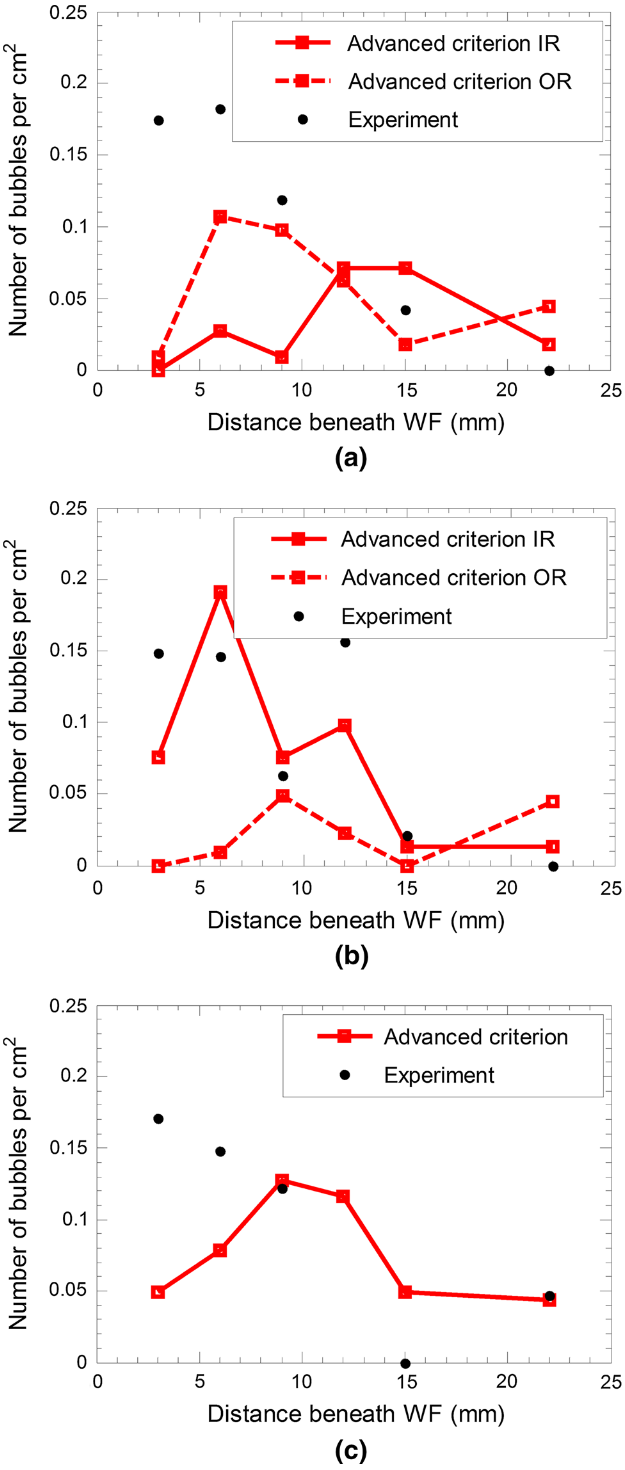

Fig. 25—Predicted number of bubbles captured per cm^2 at (*a*) center region, (*b*) quarter region, and (*c*) NF region.

flow is due to the biased gas flow caused by the argon gas slide gate moving toward the IR. The plant measurements are even stronger than the predictions. However, only two nailboard measurements of this chaotic flow were available, so perfect quantitative matching is not expected. Further measurements are needed to better quantify the steel-Ar flow pattern.

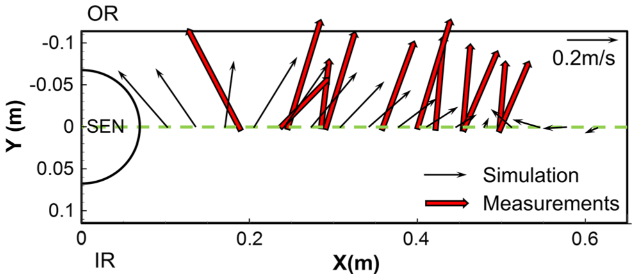

Fig. 26—Compare centerline velocity on top surface with plant measurement.

B. *Bubbles Captured in Samples*

The predicted number and average diameter of bubbles captured on each examined surface of the three samples are compared against plant measurements in Figures 27 and 28. Figures 27(a) and (b) show the predicted and measured number of bubbles captured per 150 × 150 mm^2 sample layer of the center sample and the quarter sample, respectively. In the center sample, both criteria underpredict the number of captured bubbles close to the strand surface, which means captured close to the meniscus region. At the quarter region, the advanced capture criterion predicted 20 to 40 bubbles on the first two layers of the examined surfaces, which matches the measurement of 35 bubbles. However, the simple criterion overpredicted the number of captured bubbles by ×4, especially in the second layer of the quarter sample.

Both criteria predict asymmetric capture on IR and OR. Figures 27(c) and (d) show the predicted and measured average bubble diameter (true diameters) on each examined sample layers of the center and quarter region samples. In the center region sample, the measured average bubble diameter was ~0.1 to 0.2 mm, while the simple capture criterion predicted 0.3 to 0.5 mm. The advanced criterion predicted 0.1 to 0.3 mm which is close to the measurements. In the quarter region sample, the measured average bubble diameters were 0.1 to 0.2 mm, while the simple criterion overpredicted (0.3 to 1.6 mm). The advanced capture criterion predicted 0.2 to 0.4 mm, which although not exactly matching the measurements, is much better than the simple criterion. The predicted numbers and average diameters of captured bubbles on each layer of the NF samples are shown in Figure 28. Both criteria under-predicted the number of captured bubbles close to the strand surface and overpredicted their average diameter. However, the advanced criterion exceeded the measurements by ~2 times, while the simple criterion was almost 4 times larger.

C. *Relative Capture Rate of Large Bubbles*

In all of the measured sample layers, ~500 bubbles were observed and only one large bubble (1.4 mm diameter) was observed >0.5 mm. So, the fraction of all observed captured bubbles >1 mm is ψ(1 mm) = 0.2 pct (1/500). To predict this capture fraction for >1 mm bubbles, Table II shows: the total number of bubbles injected into the domain during the particle tracking step (column 2); the number of 1 mm bubbles

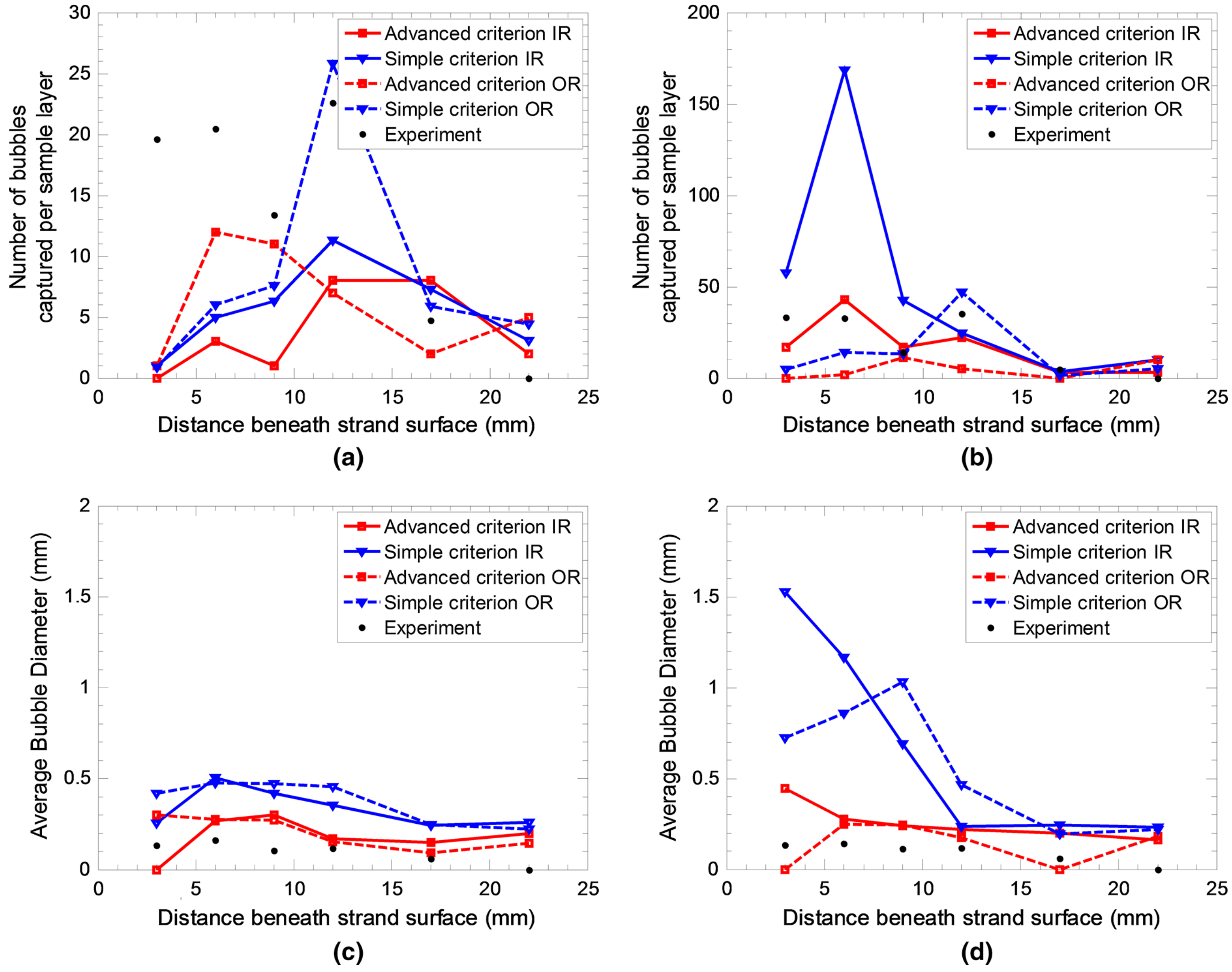

Fig. 27—Predicted number of bubbles captured in each layer of center sample (*a*) and quarter sample (*b*). Predicted average bubble diameter in center sample (*c*) and quarter sample (*d*).

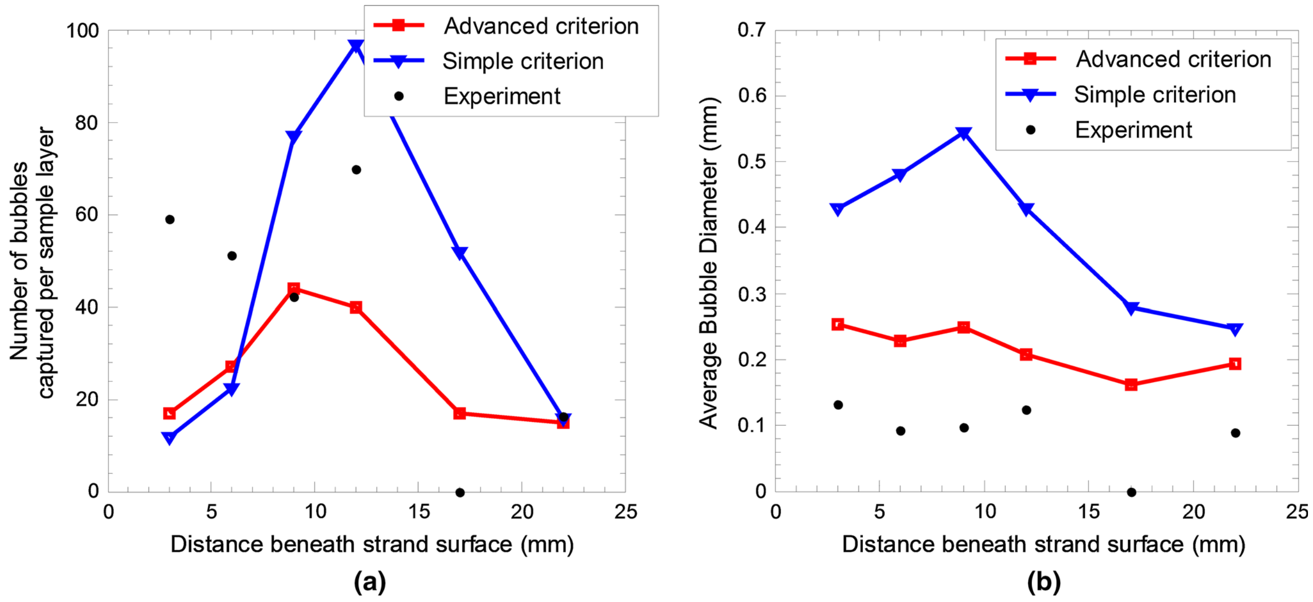

Fig. 28—Predicted (*a*) number of bubbles captured in each layer of NF sample and (*b*) corresponding average bubble diameter.

Table II. Capture Fractions of 1 mm Bubbles

Criteria	$\Sigma N(d_i)$	N (1 mm)	$\Sigma n(d_i)$	n (1 mm)	φ (1 mm)	ψ (1 mm)
Simple	2,442,390	475,640	208,944	27,799	5.84 pct	13.3 pct
Adv.	2,442,390	475,640	137,372	432	0.09 pct	0.3 pct
Exp.	unknown	unknown	~500	1	unknown	0.2 pct

injected (column 3); the total number of bubbles captured in the entire caster (column 4); the number of 1 mm bubbles captured in the entire caster (column 5); the fraction of 1 mm bubbles that was captured (column 6), and the fraction of captured bubbles that was larger than 1 mm (column 7). These results show that the advanced capture criterion prediction of 0.3 pct matches closely with the plant measurement (0.2 pct). The simple criterion greatly overpredicts the measurements (by 33×).

VI. CONCLUSIONS

The flow of molten steel, and the transport and capture of argon gas bubbles have been simulated and compared with plant measurements in a continuous slab caster. A two-way coupled Eulerian–Lagrangian model combined with a bubble tracking DRW model has been applied to predict asymmetrical flow predicted on the top surface, which agrees well with nailboard measurements. Two capture criteria were implemented, and the advanced capture criterion showed good agreement with measurements of the number, locations, and sizes of captured bubbles, especially for larger bubbles. The relative capture fraction of large (1 mm) bubbles of 0.3 pct was close to the measured 0.2 pct and occurred very near the top surface. Some important findings are summarized below:

(1) The slide gate does not cause biased crossflow at the top surface for single-phase flow. However, when Ar gas is injected with the sliding gate moving toward the IR, more Ar bubbles leave the ports toward the IR and lead to cross flow on the top surface from IR to OR, and corresponding nonuniform bubble capture on the IR and OR;
(2) Almost 85 pct of small (<0.08 mm) bubbles are captured. A very small fraction of large bubbles is captured (<0.02 pct). This fraction drops almost one order of magnitude with increasing bubble size from 1 to 2 mm and from 2 to 3 mm;
(3) The removal fraction of large bubbles ($1 \le d_\mathrm{p} \le 5$ mm) was 99.98 pct, for medium bubbles ($0.1 \le d_\mathrm{p} \le 0.3$ mm) was around 48.5 pct and for small bubbles ($d_\mathrm{p} < 0.1$ mm) was close to 15 pct;
(4) Most bubbles are captured very near to the meniscus. Deeper than 0.5 m below the meniscus, the capture fraction of medium bubbles is about half that of small bubbles;
(5) The predicted bubbles captured shows similar trends as the plant measurements, except in the first layer near to the outer surfaces, where more bubbles are captured than predicted. This might be due to the model neglecting the effects of meniscus hook capture, or assuming immediate escape of bubbles that reach the top surface.

ACKNOWLEDGMENTS

The authors thank National Science Foundation (Grant No. CMMI 11-30882) and the Continuous Casting Consortium, University of Illinois, for support of this project. Thanks are also given to Baosteel, Shanghai, P.R. China, for providing the casting conditions and measurements. This research is also part of the Blue Waters sustained-petascale computing project at the National Center for Supercomputing Applications at the University of Illinois, which is supported by the National Science Foundation (Awards OCI-0725070 and ACI-1238993) and the State of Illinois.

REFERENCES

1. AISE Steel Foundation, A.W. Cramb, and C.B. Francis: *The Making, Shaping and Treating of Steel: Casting Volume*, AISE Steel Foundation, Washington, DC, 2003.
2. H. Bai and B.G. Thomas: *Metall. Mater. Trans. B*, 2001, vol. 32B, pp. 253–67.
3. H. Bai and B.G. Thomas: *Metall. Mater. Trans. B*, 2001, vol. 32B, pp. 707–22.
4. K.G. Rackers and B.G. Thomas: *78th Steelmak. Conf. Proc.*, Iron and Steel Society, Nashville, TN, 1995, pp. 723–34.
5. J. Knoepke, M. Hubbard, J. Kelly, R. Kittridge, and J. Lucas: *Steelmak. Conf. Proc.*, Iron and Steel Society, Chicago, IL, 1994.
6. B.G. Thomas: *Iron Steel Technol.*, 2006, vol. 3, p. 127.
7. L. Zhang, J. Aoki, and B.G. Thomas: *Metall. Mater. Trans. B*, 2006, vol. 37B, pp. 361–79.
8. H.L. Yang, P. He, and Y.C. Zhai: *ISIJ Int.*, 2014, vol. 54, pp. 578–81.
9. B.G. Thomas and X. Huang: *76 Th Steelmak. Conf.*, 1993, pp. 273–89.
10. B.G. Thomas, X. Huang, and R.C. Sussman: *Metall. Mater. Trans. B*, 1994, vol. 25B, pp. 527–47.
11. C. Pfeiler, M. Wu, and A. Ludwig: *Mater. Sci. Eng. A*, 2005, vol. 413, pp. 115–20.
12. Y. Wang and L. Zhang: *Metall. Mater. Trans. B*, 2011, vol. 42B, pp. 1319–51.
13. Q. Yuan, B.G. Thomas, and S.P. Vanka: *Metall. Mater. Trans. B*, 2004, vol. 35B, pp. 703–14.
14. Q. Yuan: PhD Thesis, University of Illinois at Urbana-Champaign, 2004.
15. S. Mahmood: MS Thesis, University of Illinois at Urbana-Champaign, 2006.
16. L. Zhang and Y. Wang: *JOM*, 2012, vol. 64, pp. 1063–74.
17. B.G. Thomas, Q. Yuan, S. Mahmood, R. Liu, and R. Chaudhary: *Metall. Mater. Trans. B*, 2014, vol. 45B, pp. 22–35.
18. V. Singh, S.K. Dash, J.S. Sunitha, S.K. Ajmani, and A.K. Das: *ISIJ Int.*, 2006, vol. 46, pp. 210–18.
19. B. Li, T. Okane, and T. Umeda: *Metall. Mater. Trans. B*, 2000, vol. 31B, pp. 1491–1503.
20. R. Sanchez-Perez, L. García-Demedices, J. PalafoxRamos, M. Diaz-Cruz, and R.D. Morales: *Metall. Mater. Trans. B*, 2004, vol. 35B, pp. 85–99.

21. Z. Liu, F. Qi, B. Li, and M. Jiang: *Metall. Mater. Trans. B*, 2015, vol. 46B, pp. 933–52.
22. R.C. Sussman, M.T. Burns, X. Huang, and B.G. Thomas: *10th Process Technol. Conf. Proc.*, Iron and Steel Society, Toronto, ON, 1992, pp. 291–304.
23. Q. Yuan and B.G. Thomas: *Third Int Congr. Sci. Technol. Steelmak.*, 2005, pp. 745–62.
24. C. Pfeiler, B.G. Thomas, M. Wu, A. Ludwig, and A. Kharicha: *Steel Res. Int.*, 2008, vol. 79, pp. 599–607.
25. B.G. Thomas, A. Denissov, and H. Bai: *Steelmak. Conf. Proc.*, Iron and Steel Society of AIME, 1997, pp. 375–84.
26. Z.-Q. Liu, B.-K. Li, M.-F. Jiang, and F. Tsukihashi: *ISIJ Int.*, 2013, vol. 53, pp. 484–92.
27. E. Krepper, D. Lucas, T. Frank, H.-M. Prasser, and P.J. Zwart: *Nucl. Eng. Des.*, 2008, vol. 238, pp. 1690–1702.
28. H. Bai and B.G. Thomas: *Metall. Mater. Trans. B*, 2001, vol. 32B, pp. 1143–59.
29. C. Liu, Z. Luo, T. Zhang, D. Shen, W. Nan, and Z. Zou: *J. Iron Steel Res. Int.*, 2014, vol. 21, pp. 403–07.
30. R.C. Sussman, M.T. Burns, X. Huang, and B.G. Thomas: *Iron Steelmak.*, 1993, vol. 20, pp. 14–16.
31. Z. Liu, B. Li, and M. Jiang: *Metall. Mater. Trans. B*, 2014, vol. 45B, pp. 675–97.
32. D.R. Uhlmann, B. Chalmers, and K.A. Jackson: *J. Appl. Phys.*, 1964, vol. 35, pp. 2986–93.
33. J. Pötschke and V. Rogge: *J. Cryst. Growth*, 1989, vol. 94, pp. 726–38.
34. D. Shangguan, S. Ahuja, and D.M. Stefanescu: *Metall. Trans. A*, 1992, vol. 23A, pp. 669–80.
35. D.M. Stefanescu and A.V. Catalina: *ISIJ Int.*, 1998, vol. 38, pp. 503–05.
36. A.W. Rempel and M.G. Worster: *J. Cryst. Growth*, 1999, vol. 205, pp. 427–40.
37. Y. Wang, M. Valdez, and S. Sridhar: *Z. Für Met.*, 2002, vol. 93, pp. 12–20.
38. J.W. Garvin, Y. Yang, and H.S. Udaykumar: *Int. J. Heat Mass Transf.*, 2007, vol. 50, pp. 2969–80.
39. J.C.T. Kao, A.A. Golovin, and S.H. Davis: *J. Fluid Mech.*, 2009, vol. 625, pp. 299–320.
40. R. Liu, J. Sengupta, D. Crosbie, S. Chung, M. Trinh, and B.G. Thomas: *Sens. Sampl. Simul. Process Control*, Wiley, San Diego, 2011.
41. ANSYS Inc.: *ANSYS FLUENT 12.0 Theory Guide*. ANSYS Inc, 2009.
42. Q. Yuan, B.G. Thomas, and S.P. Vanka: *Metall. Mater. Trans. B*, 2004, vol. 35B, pp. 685–702.
43. R. Liu: Ph.D. Thesis, University of Illinois at Urbana-Champaign, 2015.
44. B.E. Launder and B.I. Sharma: *Lett. Heat Mass Transf.*, 1974, vol. 1, pp. 131–37.
45. B.E. Launder and D.B. Spalding: *Comput. Methods Appl. Mech. Eng.*, 1974, vol. 3, pp. 269–89.
46. G.-G. Lee, B.G. Thomas, and S.-H. Kim: *Met. Mater. Int.*, 2010, vol. 16, pp. 501–06.
47. R. Liu, S.-M. Cho, B.G. Thomas, and S.-H. Kim: *Continuous Casting Consortium Annual Meeting, Presentation 02*, University of Illinois at Urbana Champaign, August 16, 2015, private communication.
48. S. Morsi and A.J. Alexander: *J. Fluid Mech.*, 1972, vol. 55, pp. 193–208.
49. S.N. Lekakh, V. Thapliyal, and K. Peaslee: *2013 AISTech Conf. Proc.*, Association for Iron & Steel Technology, Pittsburgh, PA, 2013.